Intramolecular Vibrational Energy Relaxation of CO_2 in Cross-Linked Poly(ethylene glycol) Diacrylate-Based Ion Gels

C.J. Kelsheimer and Sean Garrett-Roe*

Department of Chemistry, University of Pittsburgh, 219 Parkman Avenue, Pittsburgh, PA 15260, United States

E-mail: sgr@pitt.edu

Phone: +1 412 624 1283. Fax: +1 412 624 8611

Abstract

Ultrafast two-dimensional infrared spectroscopy (2D-IR) and Fourier-transform infrared spectroscopy (FTIR) were used to measure carbon dioxide (CO_2) in 1-ethyl-3-methylimidazolium bis(trifluoromethylsulfonyl)imide ([emim][Tf_2N]), cross-linked low-molecular weight poly(ethylene glycol) diacrylate (PEGDA), and an ion gel composed of a 50 vol% blend of the two. The center frequency of the antisymmetric stretch, ν_3, of CO_2 shifts monotonically to lower wavenumbers with increasing polymer content, with the largest linewidth in the ion gel (6 cm^{-1}). Increasing polymer content slows both spectral diffusion and vibrational energy relaxation (VER) rates. An unexpected excited state absorbance peak appears in the 2D-IR of cross-linked PEGDA due to VER from the antisymmetric stretch into the bending mode, ν_2. Thirty-two response functions are necessary to describe the observed features in the 2D-IR spectra. Nonlinear least squares fitting extracts both spectral diffusion and VER rates. In the ion gel, CO_2 exhibits spectral diffusion dynamics that lie between that of the pure compounds. The kinetics of VER reflect both fast excitation and de-excitation of the bending mode, similar to the IL, and slow overall vibrational population relaxation, similar to the cross-linked polymer. The IL-like and polymer-like dynamics suggest that the CO_2 resides at the interface of the two components in the ion gel.

1 Introduction

Composite materials of ionic liquids and polymer membranes combine the selectivity of ionic liquids (ILs) with the advantages of membranes for potential next generation carbon capture technologies. Room temperature ionic liquids have emerged as potential alternatives to amine absorption systems of carbon capture.[1,2] This promise motivated the determination of both the performance limiting macroscopic properties (viscosity, thermodynamics of gas solubility, and gas transport) and investigation of the intermolecular interactions[3] that cause them.[4–6] Bulk ILs, however, have proved impractical for gas separations, largely because of their high viscosity.[1,7–9] While con-

ventional membrane-based separations work under milder conditions, consume less energy, and occupy smaller footprints than bulk amine absorbers in general,[10] they have low CO_2 / N_2 selectivity and poor gas permeability. IL-polymer composite materials can side-step these limitations, and the encapsulated IL does not need to flow. The ILs beneficially plasticize the membrane, improve gas transport, and increase the solubility selectivity.

IL-polymer composites are diverse and include ion gels,[11–13] supported ionic liquid membranes (SILMs),[14,15] and poly-ionic liquids (PILs).[16,17] These composite materials differ in the method of trapping the IL.

Ion gels are polymer films impregnated with IL. They are made by either swelling a polymer film or crosslinking a polymer in an IL-polymer mixture. Depending on miscibility, compatibility, and casting method, this process can produce a stable gel with trapped IL. Benefits of ion gels include the potential for both physical and chemical interaction between the polymer and the ionic liquid, along with commercial availability of the components. Kusuma, et al. explored their potential for CO_2 separations and showed that many properties vary with IL identity and crosslinking density.[12,13]

Supported ionic liquid membranes (SILMs) are porous polymer films that are filled with ionic liquid, which is held primarily by capillary forces.[18–20] This film construction limits carbon capture utility because large transmembrane pressures can evacuate the membrane.[9]

Poly-ionic liquids (PILs) include polymerized anions, cations, or both. PIL membranes[21] impregnated with "free IL" lie near the 2008 Robeson limit,[22] with high CO_2 permeability and relatively high CO_2/N_2 selectivity.[21] PIL membranes span a broad range of potential applications, from gas separations materials to solid electrolytes with the potential for triggerable changes.[23,24] Wide-spread implementation of PILs, however, may be limited by the film expense and complexity.[12]

To each of these composite materials, ILs add their unique properties, as ILs are structurally heterogeneous fluids. X-ray and neutron scattering experiments[25–27] supplemented by MD simulations[28–30] have established that ILs exhibit nano- or meso-

scopic ordering. The charge-carrying moieties of the cations and anions aggregate and the non-polar alkyl-chains aggregate, generating structure on multiple characteristic length-scales. The characteristic length-scales can be described in a very general way by the types of structural features on that length-scale (from short to long): adjacency, charge-alternation, and polarity alternation.[31,32]

Structural heterogeneity influences the dynamics measured in ILs.[33,34] The dynamic timescales reflect both the varied microenvironments in the liquids, and the type of interaction between the molecular reporter and the IL.[35] Short time dynamics (< 1 ns) in polar and non-polar domains can markedly be different.[36–40] The long-time dynamics (> 1 ns) reported in many kinds of spectroscopic observables involve the reorganization of the polar and non-polar domains.[41–44]

The vibrational modes of CO_2 can also serve as spectroscopic reporters of the local structure and dynamics around the CO_2. The relevant vibrational eigenstates of this system with their associated quantum numbers are the symmetric stretch, ν_1; the bend ν_2; the vibrational angular momentum, l; and the antisymmetric stretch, ν_3; denoted $|\nu_1 \nu_2^l \nu_3\rangle$. The symmetric stretch and the vibrational angular momentum play no direct role in this discussion, so we suppress their labels, for example, $|0\,0^0\,0\rangle \equiv |\nu_2\nu_3\rangle = |0\,0\rangle$.

2D-IR spectroscopy provides spectroscopic observables that are tight constraints on models of liquid structure and dynamics. Because the vibrational frequency of a molecule is most influenced by its nearest neighbors, 2D-IR can report the structure and dynamics of a probe molecule in its first solvation shell. As the solvation shell fluctuates, the vibrational frequency changes as well. The random walk in vibrational frequency space is called spectral diffusion and causes a characteristic change in the shape of 2D-IR spectra. The reorientation of a molecule with respect to the laboratory frame causes a change in the amplitude of the 2D-IR signal, as does vibrational energy relaxation. Polarization-resolved experiments can separate the effects of lifetime and reorientation on the 2D-IR spectra, providing a 2D frequency-resolved map of orientational anisotropy,[45] and can even separate the effects of structural reorganization and reorientation on the vibrational frequency fluctuations.[46,47] All of these observables can

be modeled in molecular dynamics simulations. For the case of CO_2 in an archetypal IL, the 2D-IR experimental observables provide constraints on the modeling[48,49] and the modeling provides molecular explanations of the spectroscopy.[50–53]

In bulk ILs, this kind of experimentally-validated computational investigation has revealed the mechanism of selective CO_2 solvation.[53] The IL forms a solvation shell that complements the quadrupole of the CO_2 molecule. The electrostatic interactions account for almost all the enthalpy of solvation, and the additional structure of the solvation shell explains, at least qualitatively, the negative entropy of solvation. N_2, on the other hand, does not induce this restructuring in the liquid.[53]

The dynamics in ILs change in composite materials and at interfaces in complex ways. In some experiments, interfaces, including between ILs and substrates, ILs and surrounding liquids, and ILs in composite materials, can induce changes in IL dynamics and even average structure in the IL, which can extend to remarkably long time- and lengthscales. Reflectance IR and second harmonic generation (SHG) suggest reordering of ILs under sheer flow at mica interfaces extending over micrometer lengthscales.[54] 2D-IR of IL droplets in an oil bath suggest changes in the ultrafast dynamics over micrometer lengthscales, while 2D-IR of ILs in SILMs as a function of pore size suggest that the dynamics due to the interfaces change back to the bulk values on a few tens of nanometers lengthscales.[55] This area is still actively under investigation and suggests the kinds of complex changes in structure and dynamics that can occur by incorporating ILs into more complex environments and materials.[14,15,56]

Though most 2D-IR studies focus on vibrational frequency fluctuations, both vibrational energy relaxation (VER) and the frequency fluctuation dynamics reflect the stochastic coupling of the vibrational chromophore to its bath. Both effects can be written in terms of time correlation functions of the appropriate coupling elements. In this formalism, the Fourier transform of the time correlation function of the coupling between vibrational energy levels evaluated at the frequency of their energy difference is the rate of population relaxation between the two levels, k_{ij}.[57] The spectral diffusion

dynamics can be extracted directly from the shapes of 2D-IR spectra via:

$$c_2(t) = \langle \delta\omega(t)\delta\omega(0) \rangle \,. \tag{1}$$

Here, $c_2(t)$ is the two-point frequency fluctuation correlation function, $\delta\omega(t)$ is the instantaneous fluctuation of the frequency at time t, $\omega(t)$, from the average frequency, $\langle\omega\rangle$, (i.e., $\delta\omega(t) = \omega(t) - \langle\omega\rangle$). In other words, the 2D-IR spectra report the dynamics of the system-bath coupling both in the frequency fluctuations and in the VER rate.

Because both VER and FFCFs depend on time correlations of the bath, both report the dynamics of the molecule in the fluctuating environment. There are, however, important differences in the characteristic motions that each process reports. The VER rate depends on high energy fluctuations (i.e., ω_{ij} is typically an intramolecular vibration of several thousand wavenumbers). On the other hand, c_2 typically reports only low frequency modes (i.e., the fastest timescales are typically on the order of 100 fs, corresponding to intermolecular modes on the order of < 300 cm^{-1}). This difference reflects the amount of energy exchanged with the bath, or equivalently, the density of modes (spectral density) at the relevant frequencies. In this formulation, both VER and frequency fluctuations report the stochastic dynamics of the surroundings of the spectroscopic chromophore.

VER of CO_2 in solution is often adequately described as a simple exponential loss of population in the vibrationally excited mode, occurring with a timescale T_1. The T_1 time for CO_2 in water is on the order of 10 ps.[58] In ionic liquids, vibrational relaxation rates of CO_2 are $\sim$ 60 ps.[48,59,60] The focus of this work, however, is to characterize both inter- and intramolecular flow of energy after vibrational excitation.

Previous 2D-IR experiments in ionic liquids have observed the flow of energy into and out of the bending mode reported by the antisymmetric stretch. In the linear absorption experiment, CO_2 displays a "hot-band" located ~12 cm^{-1} lower than the ν_3 antisymmetric stretching mode. This hot-band results from the anharmonic coupling of the stretch and the bend, contrary to older literature.[61] The thermal population of

the doubly degenerate state with one quantum of bend is roughly 7% at room temperature. Because the stretch and bend are coupled, the excitation of the bend causes the observed shift in the ν_3 mode. 2D-IR experiments demonstrated that equilibration occurs between the total ground state $i = |0\,0\rangle$ and the thermally-excited bend state, $j = |1\,0\rangle$.[48,62] Our investigation will build on this knowledge and expand the understanding of CO_2's VER in these complex materials.

Calculating VER from simulations remains less developed than calculating vibrational frequency trajectories and remains an open theoretical challenge. Explicit calculation of the full non-equilibrium nuclear wave-function dynamics is out of reach, so many approximate methods are being developed and tested. Dynamics on excited vibrational potentials have all the complexity as dynamics on excited electronic surfaces. High frequency ($\hbar\omega > k_BT$) modes are coupled both to a bath and to each other. As recently noted,[63] even conical intersections – in this context between vibrational states – can play a role in efficiently bringing excited state population back to the vibrational ground state in at least some cases. At the same time, there are solid grounds to expect that the appropriate correction factors can rescale non-equilibrium classical dynamics to reproduce more complex quantum calculations.[64]

Semiclassical approaches offer alternative methods to calculate VER. For example, a linearized semiclassical method based on a local harmonic approximation (LHA-LSC) has been developed to calculate VER rates for a number of solutes, including CO_2.[65] Coherence transfer and the coupling of thermal fluctuation in low-frequency modes to high frequency modes were demonstrated using a semi-classical optimized mean trajectory method.[66,67] This approach was able to reproduce the experimentally observed cross-peaks in 2D-IR spectra that arise from the thermal excitation and de-excitation of the bending mode.[48] For CO_2 in an atomic liquid, VER rates derived from classical and semiclassical simulations differ by orders of magnitude. Classical simulations produced significantly slower rates, due to the large energy mismatch between the high-frequency vibration (~ 2500 cm^{-1}) and thermal energy ($k_BT \sim 200$ cm^{-1}, where k_B is the Boltzmann constant).[65] 2D-IR experiments contain information about VER processes, and

extracting these rates offers a method of testing and validating the proposed simulation methodologies. These theoretical efforts reflect the importance of understanding VER as a fundamental step in many complex chemical processes.

Increasing knowledge about the utility of CO_2 as a probe of its local environment has prompted further exploration of its molecular scale interaction behavior. Understanding this interaction allows for more comprehensive modeling, prediction, and explanation of CO_2's behavior. As such, our strategy is to utilize CO_2 as a probe of local structure and dynamics in an ion-gel-type IL-polymer composite material, along with the corresponding parent materials. The polymer chosen was a low molecular weight cross-linked poly(ethylene glycol) diacrylate (cl-PEGDA) gel. This gel is one of many polymers of interest in carbon capture and separations applications owing largely to its very high CO_2-philicity.[68] The ionic liquid examined was 1-ethyl-3-methylimidazolium bis(trifluromethylsulfonyl)imide ([emim][Tf_2N]), an ionic liquid with previously established good solubility of, and affinity for, CO_2.[8,59] This paper will focus largely on measuring and modeling the characteristic VER in these materials. The frequency fluctuation dynamics will be addressed in a subsequent publication.

In this work, we show linear (Section 3.1) and ultrafast two-dimensional infrared spectra (Section 3.2) of CO_2 in an ionic liquid, a cross-linked polymer gel, and an ion gel. We then develop a quantitative kinetic model to understand the origins of the unexpected features in the spectra, and describe the overall model for intramolecular vibrational relaxation of CO_2 (Section 3.3).

2 Methods

2.1 Materials

Bulk 1-ethyl-3-methylimidazolium bis(trifluoromethylsulfonyl)imide ([emim][Tf_2N]) was obtained from IoLiTec (Figure 1a). Poly(ethylene glycol) diacrylate (PEGDA, M_n=700, Figure 1b) and 2,2-Dimethoxy-2-phenylacetophenone (DMPA, photo-initiator) were

obtained from Sigma Aldrich. Bone dry CO_2 gas (99.8 % purity) was obtained from Matheson TRIGAS.

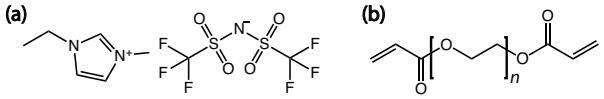

Figure 1: a) Ionic liquid 1-ethyl-3-methylimidazolium bis(trifluromethylsulfonyl)imide ([emim][Tf_2N]). b) Poly(ethylene glycol) diacrylate, $M_n = 700$ g/mol, $n \sim 14$.

2.2 Sample Preparation

Two distinct types of sample preparation were necessary. For measurements of a pure IL sample, the ionic liquid is vacuum dried prior to use, and a glove bag is utilized to control water contamination. CO_2 is loaded using a purpose-built vacuum sealed vial that enables mixing of the gaseous CO_2 and the IL. The sample is heated to ∼70 °C, and stirred while CO_2 is flowed into the vial for 10 minutes. Once loaded with CO_2, ∼1 μL is placed between CaF_2 windows separated by a 25 μm polytetrafluroethylene (PTFE) spacer, secured into a brass sample cell and then immediately placed into the N_2-purged Fourier transform infrared (FTIR) spectrometer for measurement before transferring to the 2D-IR spectrometer.

For cross-linked samples, 1% by weight DMPA is added to the desired mixture of vacuum dried parent materials, and the sample is allowed to stir for a minimum of 3 hours. Precautions are taken to prevent a premature photo-initiation. After allowing sufficient time for mixing, in a glove bag 0.5-1.5 μL of the sample mixture is placed between two CaF_2 windows, pressed to the depth of the PTFE spacer by a hollow cylinder weight, and exposed to a 36 W UV lamp (MelodySusie) for ∼2 minutes for cross-linking. To enable CO_2 loading, gels are made on drilled CaF_2 windows. To load CO_2, the custom, airtight flow cell assembly is placed into the N_2-purged FTIR spectrometer. Gas lines are attached to the cell, allowing a small pressure (< 10 kPa) of CO_2 to flow into the airtight cell and exhaust via exit tubing to atmosphere.

CO_2 uptake is monitored via the intensity of the dissolved CO_2 anti-symmetric

stretch peak ($\sim$ 2340 cm^{-1}, Figure 2). Polymer thickness was adjusted to obtain a saturated absorption of $\sim$ 0.3 O.D. For the 50 vol%, a 25 μm spacer was used. For the pure cl-PEGDA gel, a 12 μm spacer was used in order to give similar CO_2 concentrations.

2.3 Spectroscopy

FTIR spectra are taken on a N_2-purged Thermo Fischer Nicolet FTIR spectrometer, taking 4-8 scans with 0.5 cm^{-1} resolution. 2D-IR spectra are collected utilizing a Ti:Sapphire chirped pulse amplifier laser system ($\lambda = 805$ nm, 5 kHz repetition rate, 120 fs pulse duration) (Coherent Vitesse/Coherent Legend Elite). The mid-IR pulses are generated using a home-built optical parametric amplifier (OPA), designed to suppress noise.[69] After the OPA, the spectral bandwidth is around ~200 cm^{-1}. The pulses are tuned to 4.3 μm, with ~2.2 μJ entering the 2D-IR spectrometer.

The 2D-IR spectrometer employs a pump-probe geometry.[70] A Mach-Zender interferometer controls the first delay time, and a translation stage controls the second. The signal field is emitted along the path of the probe pulse. The signal, ω_3, is diffracted across a 150 l/mm grating onto a liquid N_2-cooled 2×32 channel mercury cadmium telluride detector. Signals are transmitted to the lab computer using the Femto-second Pulse Acquisition Spectrometer (IR Associates), and all data is organized and analyzed using Matlab software (MathWorks).

2.4 Global Fit Analysis

The global fitting method used to analyze and simulate experimental 2D-IR spectra utilizes response functions generated from all relevant rephasing and non-rephasing Feynman diagrams (Supporting Information). Coupled kinetic equations account for transitions between population states during t_2, and the resulting phenomenological rates account for both inter- and intramolecular vibrational relaxation processes. Orientation dynamics are accounted for by an additional set of parameters applied to these

simulated spectra. The simulated spectra are optimized using nonlinear least squares regression analysis to minimize errors. To normalize for variation in signal-to-noise ratio, the sum of square error is weighted by the number of experimental scans taken at each t_2 time. The number of scans range from 8 at early times to 120 at long times. Error bars on fitted parameters were estimated by bootstrapping[71] ($n_{\mathrm{boot}} = 100$) to obtain 95% confidence intervals on all fitted values. In bootstrapping, the global fit is repeated using random data points drawn with replacement from the full data set. The errors are estimated based on the observed variation in fitting parameters. To compare the amplitude of peaks in the experimental data and simulated spectra, the total (sum) amplitude of a selected region was plotted as a function of time. Taking a sum allowed for accurate representation of the sign of the data and accounted for any competition behavior between peaks of opposing sign.

3 Results and Discussion

3.1 Linear IR spectroscopy

In these composite materials, CO_2 senses the ionic liquid-polymer composition. CO_2's ν_3 antisymmetric stretch vibration appears near 2340 cm^{-1}, a region in both the ionic liquid and cross-linked polymer samples that is largely free of other strong absorptions (Figure 2a). Varying the composition shifts the vibrational frequency by $\sim$ 6 cm^{-1} between the pure IL (0P-100I) and cl-PEGDA (100P-0I). As the fraction of ionic liquid increases, the peak shifts linearly to higher frequency, ranging from 2337 cm^{-1} to 2342 cm^{-1} (Figure 2b,c). The width of the ν_3 band is narrowest in the 100P-0I film (4.9 cm^{-1}), broadens in the 50P-50I film (6.0 cm^{-1}), and narrows again in the 0P-100I sample (5.4 cm^{-1}).

In addition to the main band, the shoulder (hot-band) is present. A fraction of CO_2 molecules, given by the Boltzmann factor, are thermally excited to the first excited state of the bending mode. These molecules absorb at lower frequency due to the anharmonic

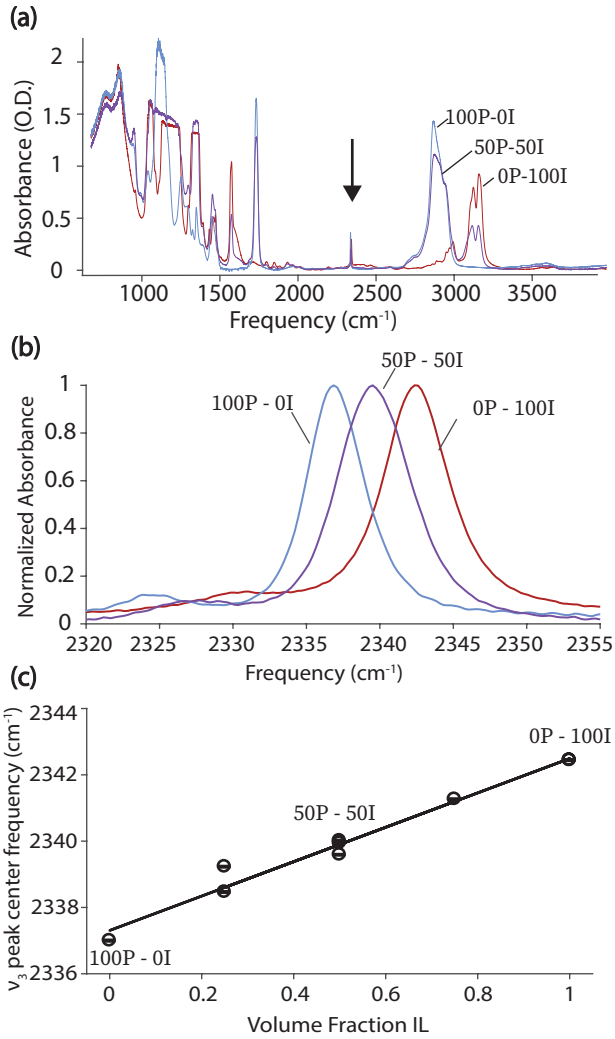

Figure 2: FTIR analysis identifies CO_2 as a strongly-absorbing, matrix-sensitive IR chromophore. a) The CO_2 peak sits in a spectrally clear region around 2340 cm^{-1} (arrow). b) The CO_2 peak shifts with changing volume percent ionic liquid. c) The CO_2 antisymmetric stretch (ν_3) peak for a series of blends are fit to a Voigt function to determine center frequency. Center frequency as a function of ionic liquid content results in a linear correlation of slope 5.2 cm^{-1} with an intercept of 2337 cm^{-1}. For each volume fraction, several mixtures were made and measured. Small compositional changes can result in differences in ν_3 frequency, especially the 0.25 and 0.50 IL fraction samples. For the 0 and 1 IL fraction samples the data markers overlap.

coupling of the antisymmetric stretch (ν_3) and the bend (ν_2). The hot-band is red-shifted by 12 cm^{-1} and has around 7% the intensity of the main antisymmetric stretch band (Figure 2b).

Solvatochromic shifts of CO_2's ν_3 vibration are seen in a variety of samples.[14,48,61,62]

Vibrational frequency decomposition[48,50] identified geometric distortion, electrostatics, and charge transfer as factors in the center frequency shift. In neat ionic liquids, geometrical distortion of CO_2 as a result of charge transfer from the anion explained the variation in vibrational frequency with anion identity. Due to the structural complexity of the mixed ionic liquid-polymer environment, similar computational studies for this system are beyond the scope of this work. Nevertheless, we can qualitatively address the influences on the vibrational frequency. A reasonable proxy for electrostatic interaction is the dielectric constant, values of which for the polymer and ionic liquids are very similar (~ 12).[72,73] This rules out electrostatics as a major contributor to the vibrational frequency shift in this system as well.

In a SILM, the CO_2 antisymmetric stretch mode split into two peaks, explained as CO_2 in two regions; the IL-filled pores and polyethersulfone (PES) polymer support. When scaled for the reduced-mass difference for the ν_3 mode in $^{12}CO_2$ and $^{13}CO_2$, the vibrational frequency is ~ 2340 cm^{-1} in the encapsulated IL ([emim][Tf_2N]) and ~ 2335 cm^{-1} in the PES.[14] (The ~ 3 cm^{-1} shift between the frequency reported in Ref.[14] and our reported value may be a result of the confinement in the polymer support, and another subtle indication of the surprisingly long range effect of IL encapsulation.) We do not see a splitting of the CO_2 peak in our work, implying a more homogeneous environment for all samples. The remaining possible explanations are that the CO_2 interacts specifically with electron rich carbonyl groups of the PEGDA in a mechanism similar to the previous ionic liquids. Alternatively, the dense packing of the film may provide a sterically constrained environment like in long-chain alkanes, which also absorb in this region, e.g. hexadecane 2335.1 cm^{-1}.[61]

3.2 Experimental 2D-IR

2D-IR measurements in the composite materials also reflect the IL-polymer ratio. 2D-IR measurements for cl-PEGDA, 100P-0I; [emim][Tf_2N], 0P-100I; and the 50 vol% ion gel, 50P-50I; were taken for t_2 values ranging from 200 fs to 250 ps (Figure 3a). All samples exhibited similar early time spectra including two diagonal peaks containing

the stimulated emission (SE) and ground state bleach (GSB) of the antisymmetric stretch and the shoulder (regions I-II, Figure 3b, blue). Also present are the two anharmonically shifted excited state absorption (ESA) peaks. For CO_2 the anharmonic shift is ~ 24 cm^{-1} (regions III-IV, Figure 3b, red). As the t_2 waiting time is increased, the peak shape changes; peaks begin inhomogenously broadened and become more rounded. This change in shape is characteristic of spectral diffusion. A quantitative analysis of spectral diffusion in these samples will be the focus of future work.

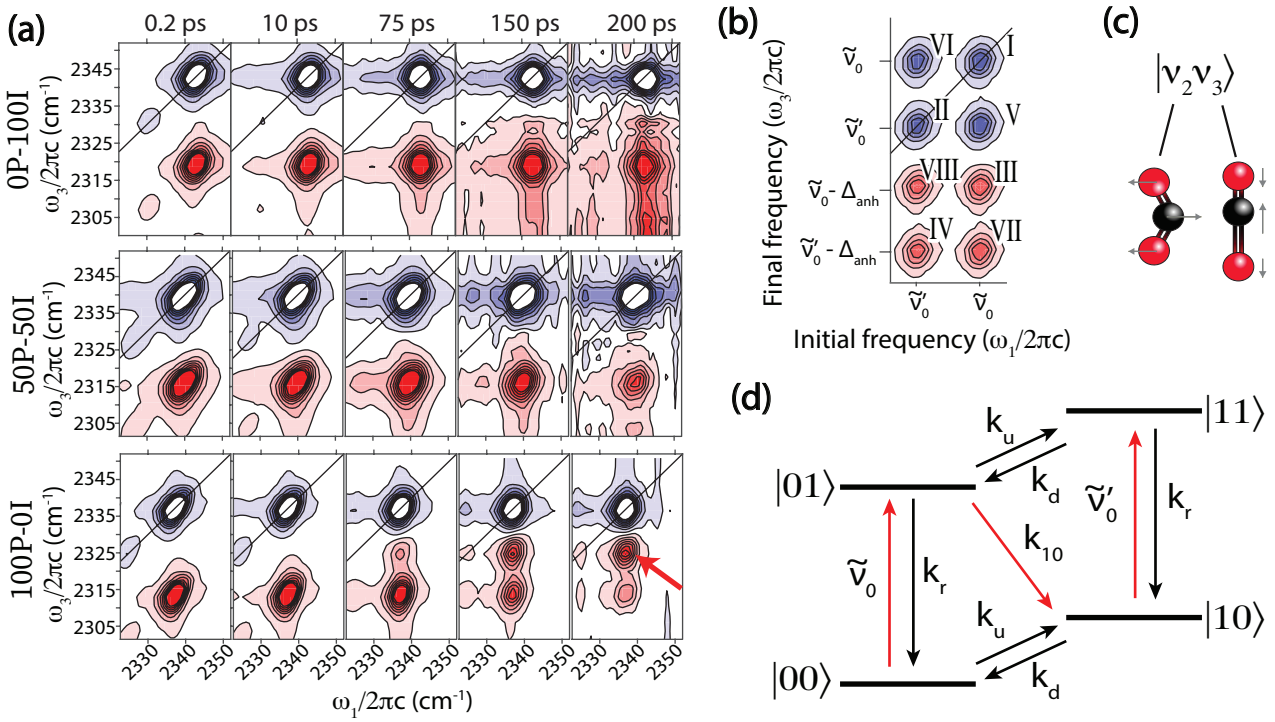

Figure 3: a) Experimental 2D-IR of CO_2 reveal an unexpected peak at long times (> 75 ps) in the 100P-0I sample (red arrow). To highlight smaller features, the fourteen contours are drawn at equally spaced intervals, centered around zero, beginning at half the most negative value. Full data sets are available in the supporting information. b) The third-order transitions of the antisymmetric stretch of CO_2 generate peaks in eight regions of the 2D-IR spectrum. c) Kets are labeled with bend and antisymmetric stretch quantum numbers. d) The energy-level diagram and kinetic rate constants. The red arrows, including the crossover pathway, k_{10} ($|0\,1\rangle$ to $|1\,0\rangle$) trace the pathway that generates the hot ground state.

The focus of this work is the dynamics of the cross-peaks and the inter- and intra-molecular vibrational energy flow that they report (Figure 3d). In general, cross-peaks appear off the diagonal and can result from mechanical or vibrational coupling,

chemical exchange, and population or coherence transfer.[74] For CO_2, cross-peaks arise from reversible population transfer between the antisymmetric stretch and the shoulder, constrained by the temperature dependent equilibrium constant, K_{eq}. By 75 ps in all samples, the shoulder peaks (regions II and IV) have disappeared due to the downhill flow of energy from $|1\,0\rangle$ to $|0\,0\rangle$ (Figure 3d, k_d).

At long t_2 times ($>$ 75 ps), the CO_2 spectrum in cl-PEGDA (100P-0I) gains an additional, unexplained red peak in region V (Figure 3a, arrow). A model of reversible energy exchange between the manifolds of states (between zero and one quantum of bend) predicts a pattern of two blue cross-peaks and two red cross-peaks. This unexpected red peak contradicts this model by appearing where a blue peak is predicted. In addition to having the opposite of the expected sign, this peak appears more slowly and eventually becomes more intense than the antisymmetric stretch's excited state absorption peak.

The unexpected red peak has the features of an excited state absorption from $|1\,0\rangle$. The red peak in region V reports an initial frequency that corresponds to the energy gap between $|0\,0\rangle$ and $|0\,1\rangle$. During t_2 a population transfer occurs, and energy moves from $|0\,1\rangle$ to $|1\,0\rangle$. Its final frequency reports the energy gap between $|1\,0\rangle$ and $|1\,1\rangle$ (Figure 3d, red arrows). This process of vibrational relaxation to a state other than the ground state is often referred to as a "hot ground state" (HGS). In this instance, some molecules initially with no quanta of bend relax not to the total ground state but to the bend excited state with one quantum of excitation.

In the condensed phase, a HGS is essentially any IR-excitation-induced photoproduct, and, as such, HGSs have been observed in many systems. This behavior has been most thoroughly explored in water and alcohols. The OH or OD stretch relaxes both directly to the ground state and indirectly through the bending mode.[75] Eventually, the energy pools in low frequency, intermolecular modes of the liquid which are anharmonically coupled to the OH/OD stretch and shift its vibrational frequency.[76–88] In a similar spirit, a HGS was used to probe dynamics in the protic ionic liquid ethylammonium nitrate (EAN).[89] Essentially the same effect has been used in other systems

to track the intramolecular flow of vibrational energy through molecules, using specific functional groups as local thermometers.[90–92] In a few remarkable cases, infrared light can even drive a photoisomerization, such as the cis-trans isomerization of HONO.[93] Prior to our exploration, there has been no report of an HGS for CO_2.

Though the intermolecular flow of energy between the bath and CO_2's bending mode had been analyzed experimentally[48,59] and theoretically,[66] this intramolecular vibrational energy flow had not been noted previously. Reversible exchange of thermal energy between $|0\,0\rangle$ and $|1\,0\rangle$ predicted a blue cross-peak in this position (Figure 3d). The appearance of this peak implies a competition between the processes that formed the hot ground state and the blue cross-peak. In the 0P-100I and 50P-50I systems, there is no distinct peak in region V, implying a balance between the pathways (Figure 3a). The same cancellation effect may also explain why the feature was not noted in ionic liquid experiments. Understanding this competition both qualitatively and quantitatively requires development of a comprehensive model that accounts for both IVR and spectral diffusion dynamics in CO_2, and is the aim of this work.

3.3 Modeling Population Transfer

To test our proposed origin for the hot ground state, we developed a detailed kinetic scheme for the states of the system that participated in population transfer during the waiting time, t_2. Spectral diffusion during t_2 obscured our efforts to extract population kinetics directly from integrating peak areas (data not shown), so we developed a quantitative model that is able to treat both spectral diffusion and population transfer on equal footings. The approach combines the kinetics of population transfer during t_2 with third-order response function formalism in the cumulant approximation.

To track the flow of energy into and out of each of the four participating population

states of CO_2, we write a kinetic rate matrix, K,

$$K = \begin{array}{c} \\ |00\rangle\langle 00| \\ |01\rangle\langle 01| \\ |10\rangle\langle 10| \\ |11\rangle\langle 11| \end{array} \begin{array}{c} \begin{array}{cccc} |00\rangle\langle 00| & |01\rangle\langle 01| & |10\rangle\langle 10| & |11\rangle\langle 11| \end{array} \\ \begin{pmatrix} -k_u & k_r & k_d & 0 \\ 0 & -k_r - k_u - k_{10} & 0 & k_d \\ k_u & k_{10} & -k_d & k_r \\ 0 & k_u & 0 & -k_r - k_d \end{pmatrix} \end{array}. \tag{2}$$

The matrix includes rate coefficients for the four important kinetic pathways (Figure 3d). Rates k_u and k_d describe the previously defined thermal excitation and de-excitation pathways. The vertical relaxation rate, k_r, represents the direct relaxation from an excited state into the corresponding ground state. The crossover rate, k_{10}, describes the relaxation of energy from $|0\,1\rangle$ to $|1\,0\rangle$, crossing between manifolds. Diagonalizing K provides the time dependence of population beginning in each vibrational state. The time-dependent kinetic equations combined with a time-dependent response function formalism generates a model capable of accurately replicating all of the features visible in the experimental data.

There are 32 double-sided Feynman diagrams needed to describe the diagonal peaks, the cross-peaks due to thermal equilibration of the bending mode, and intramolecular vibrational energy relaxation (Figure 4).

Four diagonal peaks result from six rephasing diagrams (Figure 4a,b) and six non-rephasing diagrams (Supporting Information). Pathways starting in the total vibrational ground state include SE and GSB (peak 1a), and ESA (peak 2a), and the same holds for the pathways starting with one quantum of bend excitation (peaks 1b, 2b respectively). The sign of each diagram is governed by the number of interactions from the right.

Thermal excitation and de-excitation of the bend during t_2 cause four cross-peaks, 3a/b and 4a/b, to appear (Figure 4c,d). Peaks 3a and 4a result from an upward exchange between $|0\,0\rangle$ and $|1\,0\rangle$ governed by the up rate (Figure 3d, k_u). Peaks 3b and 4b result from the opposite process, exchanging downward, governed by the down

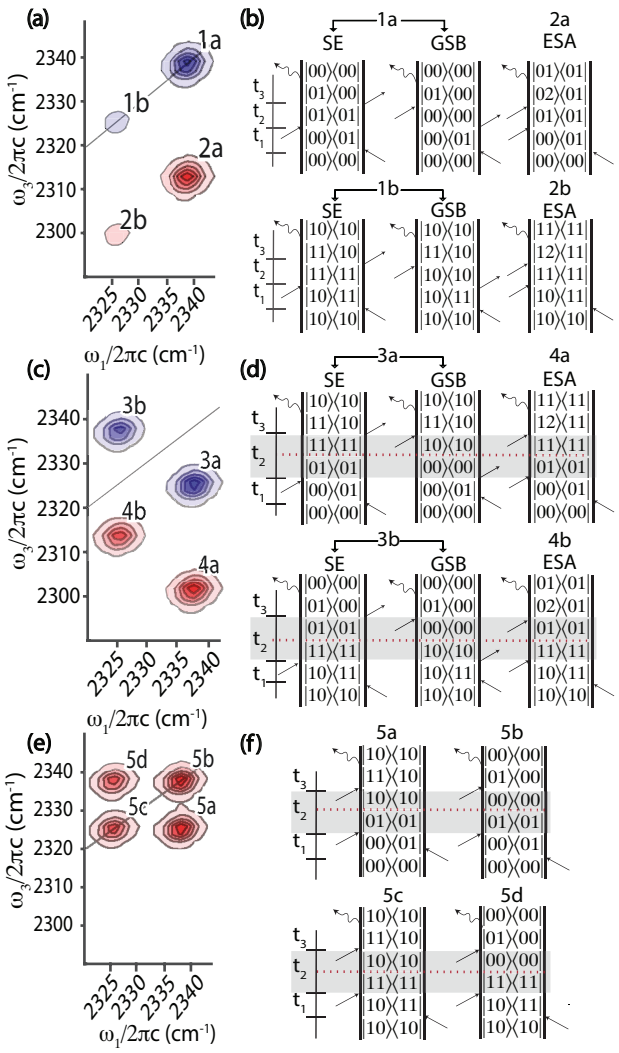

Figure 4: The 16 rephasing diagrams used to model the 2D-IR spectra. a,b) The four diagonal peaks, two from the pure antisymmetric stretch and two from the shoulder, are generated by six rephasing Feynman diagram pathways. c,d) Cross-peaks appear due to the thermal excitation and de-excitation of the bending mode during t_2 (red dashed line). e,f) Vibrational relaxation generates four peaks which overlap peaks 1a,b and 3a,b.

rate (Figure 3d, k_d). Interaction with the bath causes molecules to either gain or lose one quantum of bend, moving up or down between the two manifolds of vibrational states.

In this perturbative treatment, total vibrational relaxation causes the signal to disappear through a cancellation of terms. Without the cancellation there would be persistent blue peaks at very long times. All blue peaks are composed of SE and GSB pathways. The SE contributions scale with the population in the first excited state,

$|0\,1\rangle$, whereas GSB contributions scale with ground state population, $|0\,0\rangle$. While population in the $|0\,1\rangle$ state decreases consistently with time, population in the $|0\,0\rangle$ vibrational ground state decreases initially due to thermal equilibration with $|1\,0\rangle$, but otherwise remains constant. Because the peak in region V results from the competition between two pathways, it was necessary to fully describe the related VER pathways.

Four additional diagrams are needed to describe VER (Figure 4e,f). During t_2, energy initially deposited into the antisymmetric stretch by the laser can relax either into the bath or into a combination of the bath and other intramolecular modes. Peaks 5b and 5c reflect relaxation of energy from the antisymmetric stretching mode, leaving the number of bend quanta unchanged (none for peak 5b or one for peak 5c). Peak 5a results from population transfer between $|0\,1\rangle$ and $|1\,0\rangle$. This formally two-quantum transition is a thermal process, and optical selection rules do not govern it. This peak falls in the same location and with the same sign as the unexpected peak in the cl-PEGDA spectrum (Figure 3a, red arrow) and follows the above described pathway (Figure 3d, red arrows). Peak 5d results from energy flow from $|1\,1\rangle$ to the total vibrational ground state $|0\,0\rangle$. While this transition does not have a direct kinetic pathway in our model, there are a number of routes that energy could take during t_2 to form this peak (e.g. $|1\,1\rangle$ to $|0\,1\rangle$ via k_d and then $|0\,1\rangle$ to $|0\,0\rangle$ via k_r). These diagrams generate the four red absorption peaks that, in the long-time limit, exactly cancel the four blue ground state bleach peaks, resulting in no net 2D-IR signal.

Determining a representative lineshape function allows for accurate representation of the change in peak shape over time. In this work, we assume a two-point frequency correlation function, c_2, with a delta-function representing motions in the motional narrowing limit and an exponential for motions in the spectral diffusion regime,

$$c_2(t_2) = \frac{\delta(t_2)}{T_2} + \Delta^2 e^{-t_2/\tau}, \tag{3}$$

with fitted results for T_2, Δ, and τ. The solvent reorganization timescales decreased with increasing IL content – agreeing with previous assertions that the peak shape

appeared to change more slowly in polymer-containing samples.[14] T_2 is the dephasing time and is inversely representative of motions too fast to be captured with our experiments. T_2 decreases with increasing IL content, indicating more fast motions in the ionic liquid samples. The Δ values are a measure of frequency space sampled. In this sample set, Δ has an unexpected increase in the 50P-50I sample.

This increase in linewidth for the 50P-50I sample is also reflected in the linear spectrum (Figure 2b). It is possible that this broadening results from the the complex environment of the composite sample. Likely, this mixed-matrix sample offers a qualitatively large number of conformations and local solvation environments for CO_2 given the presence of both IL-like, polymer-like, and interfacial regions.

Our model contains several assumptions. To reduce the number of free parameters, we assume that the rate of excitation and de-excitation of the bend is the same for the ground and excited states of the antisymmetric stretch. In other words, we assume a single set of k_u and k_d suffices because the difference between $\tilde{\nu}_0$ and $\tilde{\nu}_0'$ (Figure 3d) is negligible. We also neglect potential splitting of the doubly-degenerate bending mode. In a related film, poly(methyl methacrylate), the splitting was observed to be ~ 8 cm^{-1},[94] which is negligible for our purposes.

We also employed several assumptions regarding the spectral diffusion dynamics of CO_2 which are justified based on prior work in ionic liquids. To model the lineshape, we truncate the cumulant expansion at the second order, which was shown to be a reasonable approximation.[49] We also only account for population transfer dynamics during t_2, not during t_1 or t_3, as the shoulder is well resolved and there is no coalesence of the shoulder and main band.[48] In calculating our spectra, we again employ the Condon approximation, assuming the transition dipole moment is constant with vibrational frequency.[50] Finally, we decouple rotations and frequency fluctuations. As such, the reported spectral diffusion dynamics include both reorientation-induced spectral diffusion (RISD) and structural spectral diffusion (SSD) components.[47,60]

Modeling that includes an appropriate lineshape function and accounts for population transfer kinetics reproduces the experimental data well (Figure 5). The simulated

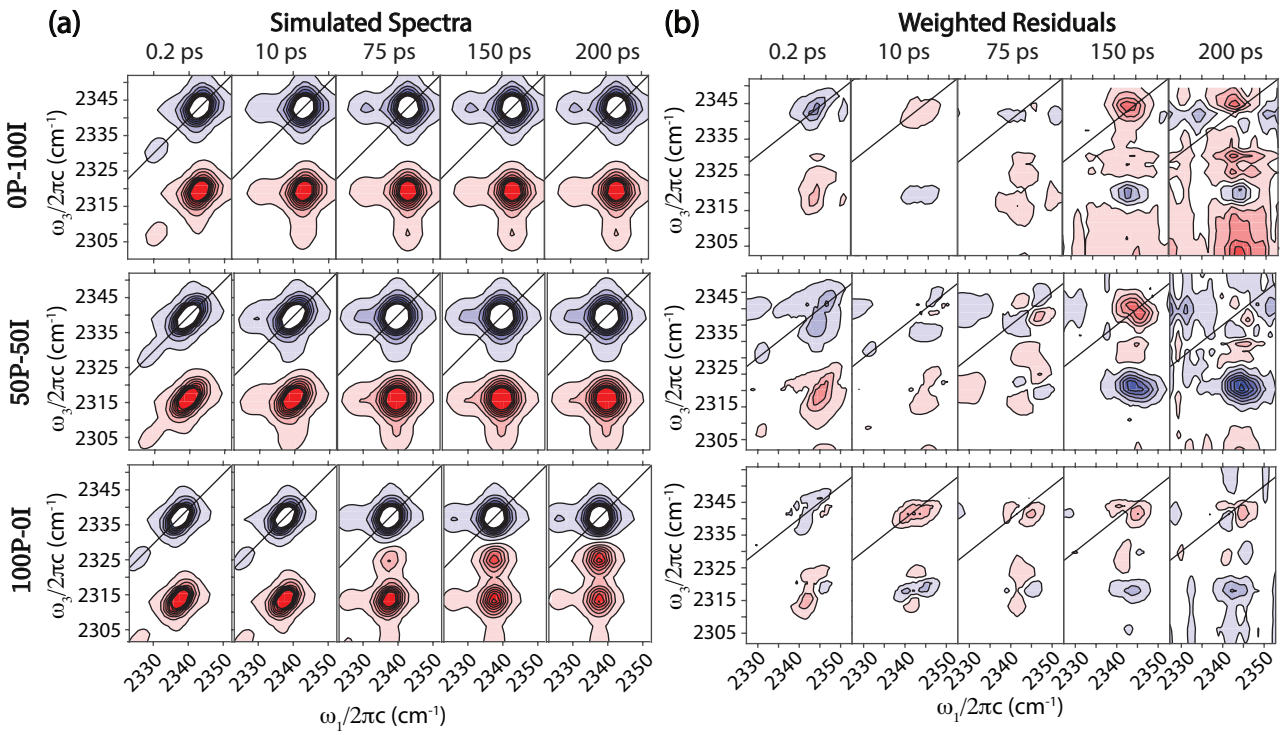

Figure 5: Kinetics-adapted response functions accurately reproduce the experimental spectra. a) The simulated spectra are shown at the same t_2 times as the experimental data, and with the same contour lines. b) Residual intensities are plotted on the same scale as the simulated spectra and experimental data.

spectra at early times include both the main diagonal antisymmetric stretch peaks and the shoulder bands with appropriate intensities (Regions I-IV). As time progresses, the cross-peaks begin to appear on reasonable timescales (Regions VI-VIII). In region V, the blue cross-peak does not appear in any of the systems with the same intensity as its counterpart in region VI, as observed in the experiment. In the 100P-0I sample, the model reflects the hot ground state peak in region V. In addition to the appropriate appearance and disappearance of peaks in the spectra, the observed spectral diffusion is reproduced.

In general, the agreement between simulated and experimental spectra is good, as the maximum intensity of appropriately weighted residuals are only around 3% of the experimental spectra for all samples. In the 50P-50I sample, the ESA decays systematically faster than in the simulated spectra. Several alternative kinetic models were explored to replicate this observation. The loss of intensity is not due to the k_{10}

pathway being reversible. We suspect that an IR-dark state is present in the system that provides an additional relaxation pathway and causes the intensity loss and is not reflected by our model. In addition to the degenerate bend (ν_2) and antisymmetric stretch (ν_3) CO_2 has a symmetric stretch (ν_1) that occurs at $\sim$ 1300 cm^{-1} but is IR-dark and would not be visible in a 2D-IR investigation. IR-pump – Raman-probe experiments, which have been demonstrated,[75] might be able to quantify this process. Nevertheless, the kinetic analysis was not sensitive to this small systematic error.

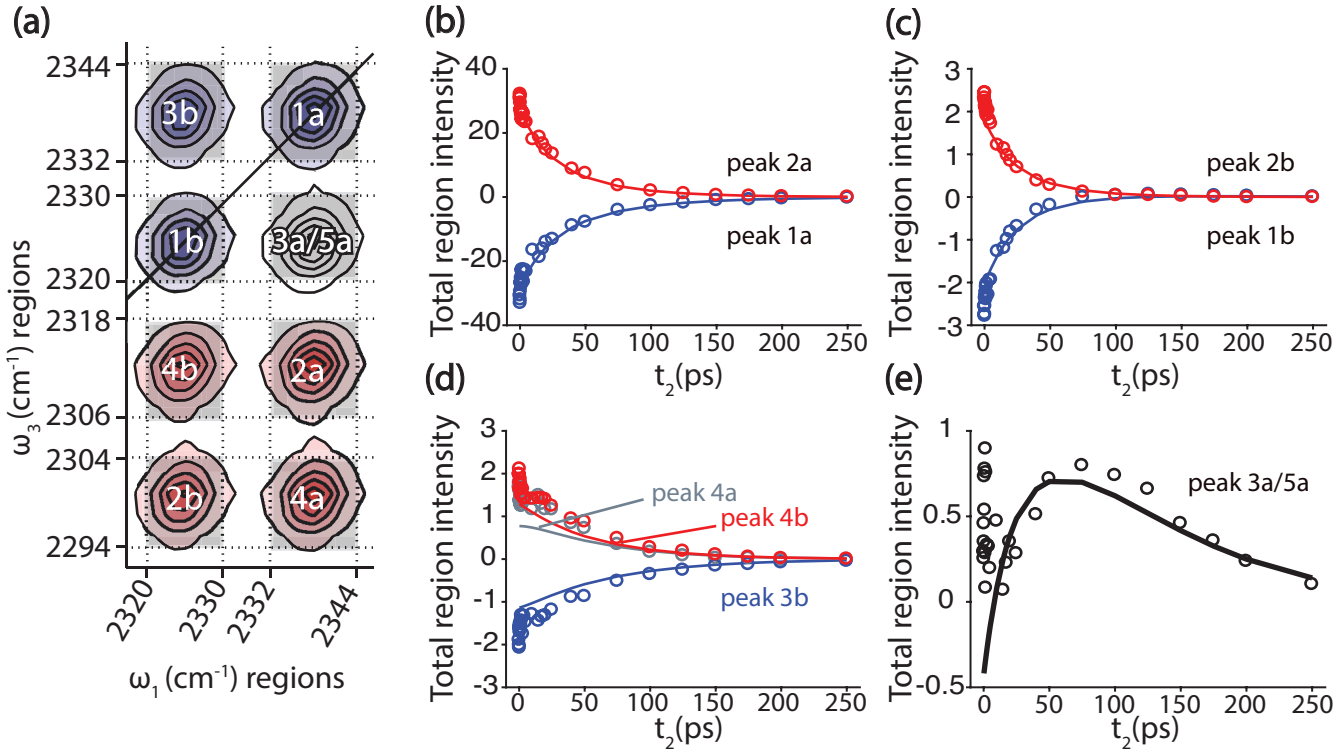

Figure 6: For the 100P-0I sample, there is good agreement between the simulated spectra and the experimental data. a) A schematic indication of the the eight regions of interest quantified in the simulated and experimental spectra. Region V, peaks 3a and 5a, can have either positive or negative sign depending on the competition of the opposing signals. b, c, d) The model (lines) and experiment (circles) agree very well for both diagonal (b,c) and cross-peaks (d). e) The fit reproduces the positive amplitude observed in the experiment because peak 5a outcompetes peak 3a.

To extract a measure of peak kinetics that could be compared to the simulated spectra, we selected each of the eight peak regions and extracted a total intensity from each spectrum (Figure 6a). Intensities of the antisymmetric stretch (1a/2a) and the

shoulder (1b/2b) diagonal peaks match (Figure 6b,c). The cross-peaks, which are more strongly impacted by peak overlap (3a/4b) and the available experimental frequency window (4a) and the presence of noise in the system, still show good agreement (Figure 6d). Region V shows variation at early times in the experimental amplitudes due to subtle differences between the experimental and simulated lineshape of the main bands (1a/2a). Once spectral diffusion begins, the simulated spectra accurately track the experimental kinetics in region V (Figure 6d). The results of this analysis for the 0P-100I and 50P-50I samples are shown in the supporting information.

Spectral diffusion times increase with polymer content (Table 1). The time constant, τ; and the dephasing time, T_2; both increase as polymer content increases. As the fraction of polymer increases, the dynamics reported by CO_2 slow.

The dephasing times in 100P-0I and 50P-50I samples are similar ($\sim$ 4.4 ps) and somewhat larger than in the pure ionic liquid (3.1 ps). The Δ value for the 50P-50I sample was significantly larger than the other two samples, implying a greater variety of local environments are explored. These spectral diffusion dynamics as a function of polymer content will be the focus of a future paper.

Table 1: Lineshape function best fit parameters

Sample	T_2	Δ (cm^{-1})	τ (ps)
100P-0I	4.5 ± 0.05	1.84 ± 0.02	82 ± 11
50P-50I	4.3 ± 0.07	2.3 ± 0.02	38 ± 4
0P-100I	3.1 ± 0.06	1.62 ± 0.05	16 ± 3

Quantitative values for each of the identified kinetic rates can be extracted from the fits (Table 2). The rates k_u, k_{10} and k_r are free parameters of the fit, and k_d was calculated using

$$K_{eq} = \frac{k_d}{k_u}, \tag{4}$$

where $K_{eq} = \exp(-\Delta E_{10-00}/k_B T)$ fixes the relationship between k_u and k_d, and the energy gap between the ground state and the bend first excited state, ΔE_{10-00}, is 667 cm^{-1}. For the 0P-100I sample, the indirect relaxation from antisymmetric excited state, $|0\,1\rangle$, through bending manifold, $|1\,0\rangle$, to the ground state, $|0\,0\rangle$, is fast enough

Table 2: Kinetics best fit parameters

Sample	k_u (ns^{-1})	τ_u (ps)	k_d (ns^{-1})	τ_d (ps)	k_{10} (ns^{-1})	τ_{10} (ps)	k_r (ns^{-1})	τ_r (ps)
100P-0I	1.2 ± 0.1	850 ± 50	14 ± 1	71 ± 4	6.2 ± 0.4	160 ± 10	14.5 ± 0.4	69 ± 2
50P-50I	18 ± 1	50 ± 4	230 ± 20	4.3 ± 0.3	13 ± 2	80 ± 10	7 ± 2	144 ± 50
0P-100I	11 ± 1	90 ± 9	130 ± 10	7 ± 1	22.2 ± 0.3	45 ± 1	-	-

that our model was unable to determine a separate rate for the direct relaxation process $|0\,1\rangle \rightarrow |0\,0\rangle$, given by k_r.

The timescales reported for the equilibrium up- and down processes of the pure IL agree with literature values. The values extracted from our sample were $\tau_u = 1/k_u =$ 94 ps and $\tau_d = 1/k_d = 7.4$ ps. Giammanco *et al.* reported values for [emim][Tf_2N] of $\tau_u = 140$ ps and $\tau_d = 13$ ps.[59] In a similar ionic liquid ([bmim][Tf_2N]), Brinzer *et al.*[95] obtained values of $\tau_u = 400$ ps and $\tau_d = 33$ ps. The rates are slower, possibly as a function of the higher viscosity.

We expected that the prominent ESA in Region V of the 100P-0I sample would indicate crossover between manifolds faster than the other samples. Fitting results depicted the opposite trend. The τ_{10} crossover rate in the 100P-0I sample is slower than the 50P-50P and 0P-100I samples by factors of 2 and 4, respectively. The τ_{10} crossover rate is also around two times slower than τ_d or the direct relaxation rate, τ_r, in the 100P-0I sample.

Vibrational relaxation rates depend on the density of accepting modes at the appropriate energy difference. Others have recognized that the FTIR absorption spectrum can sometimes serve as a reasonable proxy for the total density of states.[96,97] We examined the FTIR spectra of each sample at the frequency that corresponded to the energy gap between manifolds, ω_{cross}. In this system, the difference between $|0\,1\rangle$ and $|1\,0\rangle$ is ~ 1670 cm^{-1}. This frequency lies in the region between the strong absorptions of the PEGDA carbonyls (1700 cm^{-1}) and the Tf_2N sulfonyls (~ 1550 cm^{-1}). Assuming that the frequency of the bending mode is a constant, 667 cm^{-1}, in all samples, the amount of energy the bath must accept varies between samples because the center frequency the antisymmetric stretch shifts with composition (Figure 7a). At the ω_{cross} frequen-

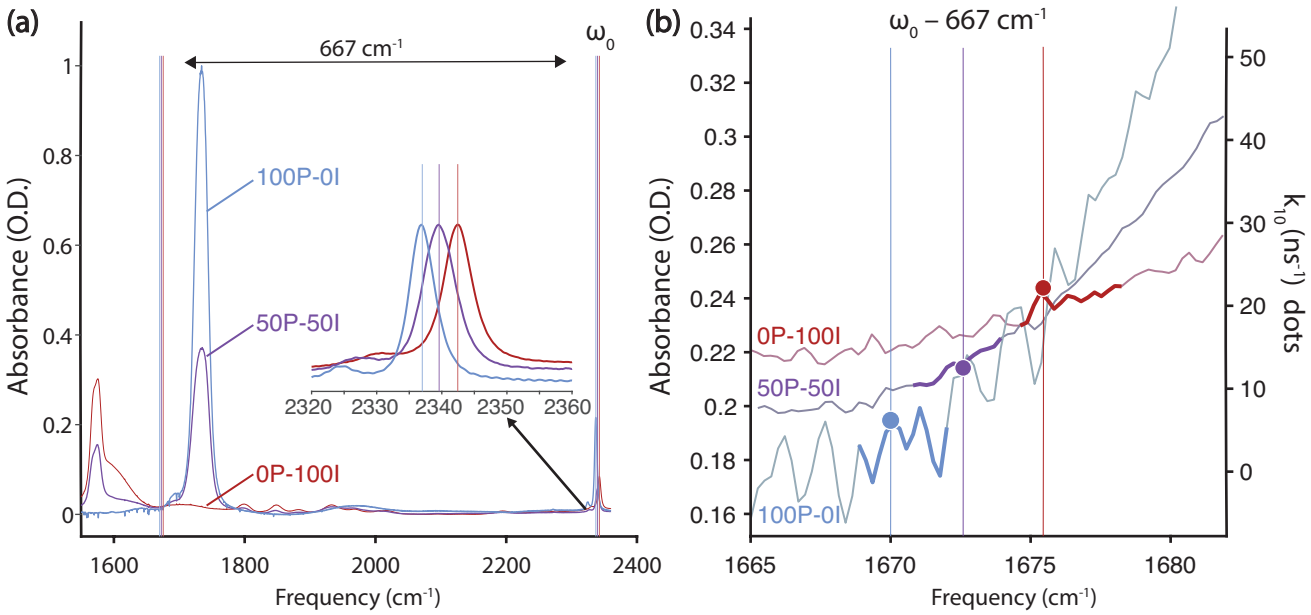

Figure 7: a) The energy gap between $|0\,1\rangle$ and $|1\,0\rangle$, $\omega_{\text{cross}} = \omega_0 - 667$ cm^{-1}, varies with IL vol%. b) k_{10} values (dots) scale relative to the background absorbance at the frequency corresponding to this energy gap. The left y-axis describes FTIR absorbance (lines), and the right y-axis describes the crossover rate (dots). Vertical lines indicate the gap frequency determined from panel (a). The FTIR of the 100P-0I contains small, sharp absorption lines that could not be removed by atmospheric correction.

cies, there are no distinct peaks, but there are differences in background absorbance. The 100P-0I sample, which had the lowest ω_{cross}, also had the lowest background absorbance and the lowest k_{10} value. The k_{10} coefficients for the 50P-50I and 0P-100I samples scaled with the background absorbance at their relative ω_{cross} values (Figure 7b). The k_{10} term reflects the capacity of the matrix to accept the energy lost in this crossover transition.

In addition to k_{10} being slow, all of the kinetic rates in the 100P-0I sample are slower than in the other samples. The largest difference is the characteristic equilibration time for the bending mode. These dynamics are constrained by the amplitudes of the peaks in regions VI and VIII. (Region VII is at the edge of the recorded spectral window in ω_3 and Region V contains signals from competing Liouville-space pathways 3a and 5a.) Chemical kinetics between two states characterized by a forward and backward rate, k_f and k_b, have a characteristic equilibration time given by the decay of the

population correlation function $k_c = k_f + k_b$, or $1/t_c = 1/t_f + 1/t_b$. Unlike the case of the k_{10} values, this characteristic equilibration time does not vary monotonically with composition. Approximating the total ground state and the first bend excited state as a two-level system, the correlation time in the 100P-0I sample is 65.7 ps which is an order of magnitude slower than in the other samples. The fastest exchange between manifolds occurs in the 50P-50I ion gel system (4 ps) which is still two times faster than the 0P-100I sample (7 ps).

A density of states explanation such as the one above for the crossover rate, k_{10}, may also explain the rapid equilibration behavior. Due to the strong absorptions of the CaF_2 windows in addition to the the sample, however, we cannot measure the vibrational density of states at the bending mode frequency ($\sim 667\ \mathrm{cm}^{-1}$) in the current experiment. 2D-IR in an attenuated total reflection (ATR) configuration[98] might be able to access this information. Lacking this information, we cannot determine if the difference in bending mode excitation and de-excitation is due to differences in the vibrational density of states or the magnitude of the system-bath coupling.

The apparent amplitude and sign of the peak in Region V depend on a subtle balance of kinetic terms. Both peak 3a (blue) and peak 5a (red) result from population in $|1\,0\rangle$ at the end of t_2. Peak 3a is a ground state bleach/stimulated emission peak and peak 5a is an excited state absorption peak. These pathways have opposite signs and can cancel. The GSB and SE diagrams must accept energy from the bath while the ESA terms must lose energy to the bath in order to transition between the two manifolds of states. Diagonalizing the kinetic matrix (Eq. 2) extracted equations for the time-dependent population of each of the four energy states that participated in population transfer during t_2. To represent the overall sign of the relevant double-sided Feynman diagrams, we assign the k_{10} pathway a positive sign, and the k_u pathways a negative sign (figure 3d). To represent the overall sign of the relevant double-sided Feynman diagrams, we assign the k_{10} pathway ($|0\,1\rangle \xrightarrow{k_{10}} |1\,0\rangle$) a positive sign, and the k_u pathway ($|00\rangle \xrightarrow{k_u} |1\,0\rangle$) and $|0\,1\rangle \xrightarrow{k_u} |1\,1\rangle$) a negative sign.

The sum of the population growth curves for these pathways reproduces the shape

of the experimental amplitude in region V (Figure 8a-c). With the exception of very early times, where peak overlap from 1a/2a influences the region, both the 100P-0I and 0P-100I samples show good agreement between the experimental data and the predicted signal. For the 50P-50P sample, the experimental signal appears to have a slightly more positive signal than is predicted by the kinetic equations. Given the small amplitude of the transients, the relatively large Δ value for this sample (Table 1), and the noise due to systematic fluctuations in the lineshape, it is likely that the total signal intensity in this region is affected by sources that are outside the scope of the kinetic predictions. Notably, however, both the 0P-100I and 50P-50I total region V intensities are smaller than the 100P-0I sample, as observed in the experiment.

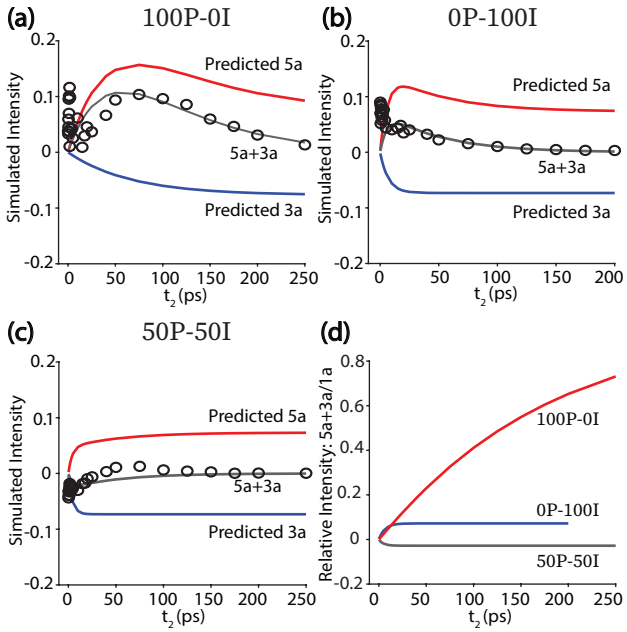

Figure 8: The relative appearance of the region V peak depends on the competition between the blue cross-peak (3a) and the red HGS peak (5a). a-c) show the population growth of the $|10\rangle$ state via the k_u pathway (Predicted 3a), and the k_{10} pathway (Predicted 5a), along with the combination of the two (grey) overlaid with a normalized experimental trace of spectral region V (points). d) Normalizing the predicted total population as a function of time (5a + 3a) by the population of the ground state exemplifies the differences between samples.

How prominent the peak in Region V appears depends on the amplitude of the peak relative to the amplitude of the peaks around it. Because the main bands are all decaying more quickly (Figure 6), the apparent or relative signal in Region V grows.

To demonstrate this effect, we normalize the predicted population in Region V by the predicted population of the ground state, Region I (Figure 8d). The relative amplitude reproduces the prominence of the red peak in Region V for the 100P-0I sample, and the very small features in the other samples. For the 100P-0I sample, there is an increasingly positive signal in region V relative to the main bands. The 50P-50I sample has a small negative signal in this region, and the 0P-100I sample has a small positive signal, but both stay very close to zero. This implies that in both the 0P-100I and 50P-50I systems, net upward exchange ($|0\,0\rangle \rightarrow |1\,0\rangle$) is very similar to the flux downward exchange ($|0\,1\rangle \rightarrow |1\,0\rangle$) of energy between the manifolds. Imbalance in these pathways, such as in the 100P-0I sample, causes the prominent hot ground state peak.

These results suggest a physical picture. The overall structural reorganization timescale in the 50P-50I sample falls between its parent compounds, but the intramolecular kinetics are more similar to the ionic liquid. This implies that CO_2's environment contains influences of both the ionic liquid and the polymer components. In other interfacial systems, reverse micelles[99–102] and planar interfaces,[98,103,104] the dynamics are different from the bulk usually within one or two solvation shells from the interface. CO_2 is known to have both a quadrupolar solvation[52] in ionic liquids, and is highly soluble in imidazolium-based ILs.[8] The room-temperature volumetric solubility, a function of the enthalpy of solution, for CO_2 in [emim][Tf_2N] is $\sim$ 2.4 $cm^3cm^{-3}atm^{-1}$.[7] For CO_2 in cross-linked PEGDA, this value is around $\sim$1.6 $cm^3cm^{-3}atm^{-1}$.[105] Given similarities between the intramolecular kinetics of the 50P-50I sample and the 0P-100I sample, and the slightly higher solubility of CO_2 in the ionic liquid, CO_2 in the ion gel sample likely localizes in a mostly-ionic liquid region that is near the polymer interface.

4 Conclusion

We utilized FTIR and 2D-IR to investigate CO_2 in a PEGDA-[emim][Tf_2N] ion gel and each parent compound. The vibrational frequency of the antisymmetric stretch,

ν_3, of CO_2 is sensitive to the composition of its environment, shifting as much as 6 cm^{-1} between the pure ionic liquid and the pure polymer. The antisymmetric stretch absorption in the 50P-50I sample is a single broad band. Rather than segregation into separate ionic liquid and polymer environments, the CO_2 likely resides near the interface of the polymer and the IL.

2D-IR experiments revealed an unexpected hot ground state in the 100P-0I sample due to intramolecular vibrational relaxation from the antisymmetric stretch into the bend. A set of 32 Liouville-space pathways describes intra- and intermolecular vibrational relaxation including thermal equilibration of the bending mode. Experimental spectra are fit to response functions that include both dynamics due to spectral diffusion and population transfer during t_2. The dephasing time (T_2) and solvent reorganization time (τ) both increase with polymer content. The Δ values for both of the pure compounds are similar, but the 50P-50I sample has a larger spread of frequencies. In an upcoming publication, we will examine the dynamics of a PEGDA-IL ion gel and the parent compounds in further detail.

VER in the pure cl-PEGDA sample occurs more slowly than in the other two. The rate of crossover from $|0\,1\rangle$ and $|1\,0\rangle$, τ_{10}, scales with background absorption at a frequency of ω_{cross}, the gap between the two states, suggesting that a difference in the vibrational density of states at the appropriate energy difference is the controlling factor. For the pure ionic liquid sample (0P-100I), the kinetics of exchange between the $|0\,0\rangle$ and $|1\,0\rangle$ states agree with literature values. The 50P-50I sample has faster between-manifolds kinetic exchange but slower total vibrational relaxation than the pure IL.

Competition between k_u, which generates a blue peak, 3a, and k_{10}, which generates a red peak, 5a, explains trends in the appearance of the hot ground state seen in the experimental data. The increased rate of exchange between manifolds in both the 0P-100I and 50P-50I samples causes approximately equal intensities of peaks 3a and 5a, leading to no observed peak in this region. This effect may explain why peak intensities in this region have been small when measured in other measurements of CO_2 in ionic

liquids.[48,59]

The molecular-level environment CO_2 experiences has already been linked to bulk properties like viscosity.[48] As such, there is much interest in investigating these environments further and in a broader scope of materials. The reported kinetics and dynamics of CO_2 in the 50 vol% ion gel reflects both IL-like and polymer-like attributes, which indicates that CO_2 is able to specifically probe the interfacial regions of this type of material. This work presents a new model for how vibrational energy is redistributed in CO_2, identifies and explains a previously unreported hot ground state of CO_2, and describes a method for extracting both kinetics and dynamics simultaneously using kinetics-adapted global fitting methods.

Supporting Information Available

Nonrephasing Feynman diagrams

Complete sets of spectra for each of the three samples

Peak area versus time plots for 50P-50I and 0P-100I samples

Details of response function generation and global fitting methodology

Acknowledgement

The authors acknowledge financial support from the National Science Foundation (CHE-1454105). C.J. Kelsheimer acknowledges funding from the Science, Mathematics and Research for Transformation Scholarship (2016-present). C.J. Kelsheimer also thanks Thomas Gasmire of the University of Pittsburgh Dietrich School of Arts and Sciences Machine Shop, Dr. Jennifer Laaser, Dr. Thomas Brinzer, Ms. Sunayana Mitra and Mr. Kai Gronborg for their assistance.

References

(1) Karadas, F.; Atilhan, M.; Aparicio, S. Review on the Use of Ionic Liquids (ILs) as Alternative Fluids for CO2 Capture and Natural Gas Sweetening. *Energy Fuels* **2010**, *24*, 5817–5828.

(2) Bhown, A. S.; Freeman, B. C. Analysis and Status of Post-Combustion Carbon Dioxide Capture Technologies. *Environ. Sci. Technol.* **2011**, *45*, 8624–8632.

(3) Kerlé, D.; Ludwig, R.; Geiger, A.; Paschek, D. Temperature Dependence of the Solubility of Carbon Dioxide in Imidazolium-Based Ionic Liquids. *J. Phys. Chem. B* **2009**, *113*, 12727–12735.

(4) Carvalho, P. J.; Alvarez, V. H.; Schröder, B.; Gil, A. M.; Marrucho, I. M.; Aznar, M.; Santos, L. M. N. B. F.; Coutinho, J. A. P. Specific Solvation Interactions of CO2 on Acetate and Trifluoroacetate Imidazolium Based Ionic Liquids at High Pressures. *J. Phys. Chem. B* **2009**, *113*, 6803–6812.

(5) Kroon, M. C.; Karakatsani, E. K.; Economou, I. G.; Witkamp, G.-J.; Peters, C. J. Modeling of the Carbon Dioxide Solubility in Imidazolium-Based Ionic Liquids with the tPC-PSAFT Equation of State. *J. Phys. Chem. B* **2006**, *110*, 9262–9269.

(6) Tomé, L. C.; Florindo, C.; Freire, C. S. R.; Rebelo, L. P. N.; Marrucho, I. M. Playing With Ionic Liquid Mixtures to Design Engineered CO2 Separation Membranes. *Phys. Chem. Chem. Phys.* **2014**, *16*, 17172–17182.

(7) Bara, J. E.; Carlisle, T. K.; Gabriel, C. J.; Finotello, A.; Gin, D. L.; Noble, R. D.; Camper, D. Guide to CO2 Separations in Imidazolium-Based Room-Temperature Ionic Liquids. **2009**, 2739–2751.

(8) Cadena, C.; Anthony, J. L.; Shah, J. K.; Morrow, T. I.; Brennecke, J. F.; Maginn, E. J. Why is CO2 So Soluble in Imidazolium-Based Ionic Liquids? *J. Am. Chem. Soc.* **2004**, *126*, 5300–5308.

(9) Bara, J. E.; Camper, D. E.; Gin, D. L.; Noble, R. D. Room-Temperature Ionic Liquids and Composite Materials: Platform Technologies for CO2 Capture. *Acc. Chem. Res.* **2010**, *43*, 152–159.

(10) Rufford, T. E.; Smart, S.; Watson, G. C. Y.; Graham, B. F.; Boxall, J.; da Costa, J. C. D.; May, E. F. The Removal of CO2 and N2 From Natural Gas: A Review of Conventional and Emerging Process Technologies. *J. Pet. Sci. Eng.* **2012**, *94-95*, 123–154.

(11) Dai, Z.; Noble, R. D.; Gin, D. L.; Zhang, X.; Deng, L. Combination of Ionic Liquids With Membrane Technology: A New Approach for CO2 Separation. *J. Memb. Sci.* **2016**, *497*, 1–20.

(12) Kusuma, V. A.; Macala, M. K.; Liu, J.; Marti, A. M.; Hirsch, R. J.; Hill, L. J.; Hopkinson, D. Ionic liquid Compatibility in Polyethylene Oxide/Siloxane Ion Gel Membranes. *J. Memb. Sci.* **2018**, *545*, 292–300.

(13) Kusuma, V. A.; Chen, C.; Baker, J. S.; Macala, M. K.; Hopkinson, D. The Effect of Poly(Ethylene oxide) Cross-Linking Structure on the Mechanical Properties and CO2 Separation Performance of an Ion Gel Membrane. *Polymer (Guildf).* **2019**, *180*, 121666.

(14) Shin, J. Y.; Yamada, S. A.; Fayer, M. D. Carbon Dioxide in a Supported Ionic Liquid Membrane: Structural and Rotational Dynamics Measured with 2D IR and Pump–Probe Experiments. *J. Am. Chem. Soc.* **2017**, 11222–11232.

(15) Shin, J. Y.; Yamada, S. A.; Fayer, M. D. Dynamics of a Room Temperature Ionic Liquid in Supported Ionic Liquid Membranes vs the Bulk Liquid: 2D IR and Polarized IR Pump–Probe Experiments. *J. Am. Chem. Soc.* **2017**, *139*, 311–323.

(16) Tome, L. C.; Gouveia, A. S. L.; Freire, C. S. R.; Mecerreyes, D.; Marrucho, I. M. Polymeric Ionic Liquid-Based Membranes: Influence of Polycation Variation on Gas Transport and CO2 Selectivity Properties. *J. Memb. Sci.* **2015**, *486*, 40–48.

(17) Ansaloni, L.; Nykaza, J. R.; Ye, Y.; Elabd, Y. A.; Giacinti Baschetti, M. Influence of Water Vapor on the Gas Permeability of Polymerized Ionic Liquids Membranes. *J. Memb. Sci.* **2015**, *487*, 199–208.

(18) Scovazzo, P.; Visser, A. E.; Davis, J. H.; Rogers, R. D.; Koval, C. A.; DuBois, D. L.; Noble, R. D. In *Ion. Liq. Ind. Appl. Green Chem.*; Rogers, R. D., Seddon, K. R., Eds.; American Chemical Society, 2002; pp 69–87.

(19) Scovazzo, P.; Kieft, J.; Finan, D. A.; Koval, C.; DuBois, D.; Noble, R. Gas Separations Using Non-Hexafluorophosphate [PF6]- Anion Supported Ionic Liquid Membranes. *J. Memb. Sci.* **2004**, *238*, 57–63.

(20) Baltus, R. E.; Counce, R. M.; Culbertson, B. H.; Luo, H.; DePaoli, D. W.; Dai, S.; Duckworth, D. C. Examination of the Potential of Ionic Liquids For Gas Separations. *Sep. Sci. Technol.* **2005**, *40*, 525–541.

(21) Cowan, M. G.; Gin, D. L.; Noble, R. D. Poly(ionic liquid)/Ionic Liquid Ion-Gels with High "Free" Ionic Liquid Content: Platform Membrane Materials for CO2/Light Gas Separations. *Acc. Chem. Res.* **2016**, *49*, 724–732.

(22) Robeson, L. M. The Upper Bound Revisited. *J. Memb. Sci.* **2008**, *320*, 390–400.

(23) Liang, J.; Xu, K.; Arora, S.; Laaser, J. E.; Fullerton-Shirey, S. K. Ion-Locking in Solid Polymer Electrolytes for Reconfigurable Gateless Lateral Graphene p-n Junctions. *Materials* **2020**, *13*.

(24) Arora, S.; Liang, J.; Fullerton-Shirey, S. K.; Laaser, J. E. Triggerable Ion Release in Polymerized Ionic Liquids Containing Thermally Labile Diels-Alder Linkages. *ACS Mater. Lett.* **2020**, 331–335.

(25) Triolo, A.; Russina, O.; Bleif, H.-J.; Di Cola, E. Nanoscale Segregation in Room Temperature Ionic Liquids. *J. Phys. Chem. B* **2007**, *111*, 4641–4644.

(26) Hardacre, C.; Holbrey, J. D.; Mullan, C. L.; Youngs, T. G. A.; Bowron, D. T. Small Angle Neutron Scattering from 1-alkyl-3-methylimidazolium Hexafluorophosphate Ionic Liquids ($[C_n mim][PF_6]$, n=4, 6, and 8). *J. Chem. Phys.* **2010**, *133*, 74510.

(27) Russina, O.; Triolo, A.; Gontriani, L.; Caminiti, R. Mesoscopic Structural Heterogeneities in Room-Temperature Ionic Liquids. *J. Phys. Chem. B* **2011**, *3*, 27–33.

(28) Urahata, S. M.; Ribeiro, M. C. C. Structure of Ionic Liquids of 1-alkyl-3-methylimidazolium cations: A Systematic Computer Simulation Study. *J. Chem. Phys.* **2004**, *120*, 1855–1863.

(29) Wang, Y.; Voth, G. A. Unique Spatial Heterogeneity in Ionic Liquids. *J. Am. Chem. Soc.* **2005**, *127*, 12192–12193.

(30) Canongia Lopes, J. N. A.; Pádua, A. A. H. Nanostructural Organization in Ionic Liquids. *J. Phys. Chem. B* **2006**, *110*, 3330–3335.

(31) Araque, J. C.; Hettige, J. J.; Margulis, C. J. Modern Room Temperature Ionic Liquids, a Simple Guide to Understanding Their Structure and How It May Relate to Dynamics. *J. Phys. Chem. B* **2015**, *119*, 12727–12740.

(32) Shimizu, K.; Bernardes, C. E. S.; Canongia Lopes, J. N. Structure and Aggregation in the 1-Alkyl-3-Methylimidazolium Bis(trifluoromethylsulfonyl)imide Ionic Liquid Homologous Series. *J. Phys. Chem. B* **2014**, *118*, 567–576.

(33) Castner, E. W., Jr.; Wishart, J. F. Spotlight on Ionic Liquids. *J. Chem. Phys.* **2010**, *132*, 120901.

(34) Castner, E. W., Jr.; Wishart, J. F.; Shirota, H. Intermolecular Dynamics, Interactions, and Solvation in Ionic Liquids. *Acc. Chem. Res.* **2007**, *40*, 1217–1227.

(35) Jin, H.; Li, X.; Maroncelli, M. Heterogeneous Solute Dynamics in Room Temperature Ionic Liquids. *J. Phys. Chem. B* **2007**, *111*, 13473–13478.

(36) Dutta, S.; Ren, Z.; Brinzer, T.; Garrett-Roe, S. Two-dimensional ultrafast vibrational spectroscopy of azides in ionic liquids reveals solute-specific solvation. *Phys. Chem. Chem. Phys.* **2015**, *17*, 26575–26579.

(37) Fruchey, K.; Lawler, C. M.; Fayer, M. D. Investigation of Nanostructure in Room Temperature Ionic Liquids using Electronic Excitation Transfer. *J. Phys. Chem. B* **2012**, *116*, 3054–3064.

(38) Fruchey, K.; Fayer, M. D. Dynamics in Organic Ionic Liquids in Distinct Regions Using Charged and Uncharged Orientational Relaxation Probes. *J. Phys. Chem. B* **2010**, *114*, 2840–2845.

(39) Xiao, D.; Rajian, J. R.; Hines, L. G., Jr.; Li, S.; Bartsch, R. A.; Quitevis, E. L. Nanostructural Organization and Anion Effects in the Optical Kerr Effect Spectra of Binary Ionic Liquid Mixtures. *J. Phys. Chem. B* **2008**, *112*, 13316–13325.

(40) Dahl, K.; Sando, G. M.; Fox, D. M.; Sutto, T. E.; Owrutsky, J. C. Vibrational Spectroscopy and Dynamics of Small Anions in Ionic Liquid Solutions. *J. Chem. Phys.* **2005**, *123*, 084504.

(41) Daguenet, C.; Dyson, P. J.; Krossing, I.; Oleinikova, A.; Slattery, J.; Wakai, C.; Weingärtner, H. Dielectric Response of Imidazolium-Based Room-Temperature Ionic Liquids. *J. Phys. Chem. B* **2006**, *110*, 12682–12688.

(42) Yamada, S. A.; Bailey, H. E.; Tamimi, A.; Li, C.; Fayer, M. D. Dynamics in a Room-Temperature Ionic Liquid from the Cation Perspective: 2D IR Vibrational Echo Spectroscopy. *J. Am. Chem. Soc.* **2017**, *139*, 2408–2420.

(43) Sonnleitner, T.; Turton, D. A.; Waselikowski, S.; Hunger, J.; Stoppa, A.; Walther, M.; Wynne, K.; Buchner, R. Dynamics of RTILs : A Comparative Dielectric and OKE study. *J. Mol. Liq.* **2014**, *192*, 19–25.

(44) Turton, D. A.; Hunger, J.; Stoppa, A.; Hefter, G.; Thoman, A.; Walther, M.; Buchner, R.; Wynne, K. Dynamics of Imidazolium Ionic Liquids from a Com-

bined Dielectric Relaxation and Optical Kerr Effect Study: Evidence for Mesoscopic Aggregation. *J. Am. Chem. Soc.* **2009**, *131*, 11140–11146.

(45) Ramasesha, K.; Roberts, S. T.; Nicodemus, R. A.; Mandal, A.; Tokmakoff, A. Ultrafast 2D IR Anisotropy of Water Reveals Reorientation During Hydrogen-Bond Switching. *J. Chem. Phys.* **2011**, *135*, 54509.

(46) Kramer, P. L.; Nishida, J.; Giammanco, C. H.; Tamimi, A.; Fayer, M. D. Observation and Theory of Reorientation-Induced Spectral Diffusion in Polarization-Selective 2D IR Spectroscopy. *J. Chem. Phys.* **2015**, *142*, 184505.

(47) Kramer, P. L.; Nishida, J.; Fayer, M. D. Separation of Experimental 2D IR Frequency-Frequency Correlation Functions Into Structural and Reorientation-Induced Contributions. *J. Chem. Phys.* **2015**, *143*, 124505.

(48) Brinzer, T.; Berquist, E. J.; Ren, Z.; Dutta, S.; Johnson, C. A.; Krisher, C. S.; Lambrecht, D. S.; Garrett-Roe, S. Ultrafast Vibrational Spectroscopy (2D-IR) of CO2 in Ionic Liquids: Carbon Capture from Carbon Dioxide's Point of View. *J. Chem. Phys.* **2015**, *142*, 212425.

(49) Brinzer, T.; Daly, C. A., Jr.; Allison, C.; Garrett-Roe, S.; Corcelli, S. A. Modeling Carbon Dioxide Vibrational Frequencies in Ionic Liquids: III. Dynamics and Spectroscopy. *J. Phys. Chem. B* **2018**, *122*, 8931–8942.

(50) Berquist, E. J.; Daly, C. A., Jr.; Brinzer, T.; Bullard, K. K.; Campbell, Z. M.; Corcelli, S. A.; Garrett-Roe, S.; Lambrecht, D. S. Modeling Carbon Dioxide Vibrational Frequencies in Ionic Liquids: I. Ab Initio Calculations. *J. Phys. Chem. B* **2017**, *121*, 208–220.

(51) Daly, C. A., Jr.; Berquist, E. J.; Brinzer, T.; Garrett-Roe, S.; Lambrecht, D. S.; Corcelli, S. A. Modeling Carbon Dioxide Vibrational Frequencies in Ionic Liquids: II. Spectroscopic Map. *J. Phys. Chem. B* **2016**, *120*, 12633–12642.

(52) Daly, C. A., Jr.; Brinzer, T.; Allison, C.; Garrett-Roe, S.; Corcelli, S. A. Enthalpic Driving Force for the Selective Absorption of CO2 by an Ionic Liquid. *J. Phys. Chem. Lett.* **2018**, *9*, 1393–1397.

(53) Daly, C. A., Jr.; Allison, C.; Corcelli, S. A. Modeling Carbon Dioxide Vibrational Frequencies in Ionic Liquids: IV. Temperature Dependence. *J. Phys. Chem. B* **2019**, *123*, 3797–3803.

(54) Anaredy, R. S.; Shaw, S. K. Long-Range Ordering of Ionic Liquid Fluid Films. *Langmuir* **2016**, *32*, 5147–5154.

(55) Tracy, K. M.; Guchhait, B.; Tibbetts, C.; Luther, B. M.; Krummel, A. Visualizing Chemical Dynamics in an Ionic Liquid Microdroplet using Ultrafast 2D IR Microscopy. *ChemRxiv* **2019**, 10.26434/CHEMRXIV.9936464.V1.

(56) Thomaz, J. E.; Bailey, H. E.; Fayer, M. D. The Influence of Mesoscopic Confinement on the Dynamics of Imidazolium-Based Room Temperature Ionic Liquids in Polyether Sulfone Membranes. *J. Chem. Phys.* **2017**, *147*.

(57) Oxtoby, D. W. Vibrational Relaxation in Liquids. *Annu. Rev. Phys. Chem.* **1981**, *32*, 77–101.

(58) Hamm, P.; Lim, M.; Hochstrasser, R. M. Vibrational Relaxation and Dephasing of Small Molecules Strongly Interacting with Water. Ultrafast Phenom. XI. BERLIN, 1998; pp 514–516.

(59) Giammanco, C. H.; Kramer, P. L.; Yamada, S. A.; Nishida, J.; Tamimi, A.; Fayer, M. D. Coupling of Carbon Dioxide Stretch and Bend Vibrations Reveals Thermal Population Dynamics in an Ionic Liquid. *J. Phys. Chem. B* **2016**, *120*, 549–556.

(60) Giammanco, C. H.; Kramer, P. L.; Yamada, S. A.; Nishida, J.; Tamimi, A.; Fayer, M. D. Carbon dioxide in an Ionic Liquid: Structural and Rotational Dynamics. *J. Chem. Phys.* **2016**, *144*, 104506.

(61) Cunliffe-Jones, D. B. Perturbation of Some Vibrational Bands in Solution. *Spectrochim. Acta Part A* **1969**, *25*, 779.

(62) Giammanco, C. H.; Yamada, S. A.; Kramer, P. L.; Tamimi, A.; Fayer, M. D. Structural and Rotational Dynamics of Carbon Dioxide in 1-Alkyl-3-methylimidazolium Bis(trifluoromethylsulfonyl)imide Ionic Liquids: The Effect of Chain Length. *J. Phys. Chem. B* **2016**, *120*, 6698–6711.

(63) Hamm, P.; Stock, G. Vibrational Conical Intersections as a Mechanism of Ultrafast Vibrational Relaxation. *Phys. Rev. Lett.* **2012**, *109*, 173201.

(64) Stock, G. Classical Simulation of Quantum Energy Flow in Biomolecules. *Phys. Rev. Lett.* **2009**, *102*, 118301.

(65) Ka, B. J.; Geva, E. Vibrational Energy Relaxation of Polyatomic Molecules in Liquid Solution via the Linearized Semiclassical Method. *J. Phys. Chem. A* **2006**, *110*, 9555–9567.

(66) Alemi, M.; Loring, R. F. Vibrational Coherence and Energy Transfer in Two-Dimensional Spectra ith the Optimized Mean-Trajectory Approximation. *J. Chem. Phys.* **2015**, *142*, 212417.

(67) Ramesh, P.; Loring, R. F. Thermal Population Fluctuations in Two-Dimensional Infrared Spectroscopy Captured with Semiclassical Mechanics. *J. Phys. Chem. B* **2018**, *122*, 3647–3654.

(68) Kilic, S.; Michalik, S.; Wang, Y.; Johnson, J. K.; Enick, R. M.; Beckman, E. J. Phase Behavior of Oxygen-Containing Polymers in CO2. *Macromolecules* **2007**, *40*, 1332–1341.

(69) Hamm, P.; Kaindl, R. A.; Stenger, J. Noise Suppression in Femtosecond Mid-Infrared Light Sources. *Opt. Lett.* **2000**, *25*, 1798–1800.

(70) Helbing, J.; Hamm, P. Compact Implementation of Fourier Transform Two-Dimensional IR Spectroscopy Without Phase Ambiguity. *J. Opt. Soc. Am. B* **2011**, *28*, 171.

(71) Press, W. H.; Teukolsky, S. A.; Vetterlin, W. T.; Flannery, B. P. *Numerical Recipes in C*, 2nd ed.; Cambridge University Press: New York, 1992.

(72) Kalakkunnath, S.; Kalika, D. S.; Lin, H.; Raharjo, R. D.; Freeman, B. D. Molecular relaxation in cross-linked poly(ethylene glycol) and poly(propylene glycol) diacrylate networks by dielectric spectroscopy. *Polymer (Guildf).* **2007**, *48*, 579–589.

(73) Singh, T.; Kumar, A. Static Dielectric Constant of Room Temperature Ionic Liquids: Internal Pressure and Cohesive Energy Density Approach. *J. Phys. Chem. B* **2008**, *112*, 12968–12972.

(74) Hamm, P.; Zanni, M. T. *Concepts and Methods of 2D Infrared Spectroscopy*; Cambridge University Press: New York, NY, 2011.

(75) Pakoulev, A.; Wang, Z. H.; Pang, Y. S.; Dlott, D. D. Vibrational Energy Relaxation Pathways of Water. *Chem. Phys. Lett.* **2003**, *380*, 404–410.

(76) Stenger, J.; Madsen, D.; Hamm, P.; Nibbering, E. T. J.; Elsaesser, T. A Photon Echo Peak Shift Study of Liquid Water. *J. Phys. Chem. A* **2002**, *106*, 2341–2350.

(77) Madsen, D.; Stenger, J.; Dreyer, J.; Hamm, P.; Nibbering, E. T. J.; Elsaesser, T. Femtosecond Mid-Infrared Pump–Probe Study of Wave Packet Motion in a Medium-Strong Intramolecular Hydrogen Bond. *Bull. Chem. Soc. Jpn.* **2002**, *75*, 909–917.

(78) Asbury, J. B.; Steinel, T.; Stromberg, C.; Gaffney, K. J.; Piletic, I. R.; Fayer, M. D. Hydrogen Bond Breaking Probed with Multidimensional Stimulated Vibrational Echo Correlation Spectroscopy. *J. Chem. Phys.* **2003**, *119*, 12981–12997.

(79) Steinel, T.; Asbury, J. B.; Zheng, J.; Fayer, M. D. Watching Hydrogen Bonds Break: A Transient Absorption Study of Water. *J. Phys. Chem. A* **2004**, *108*, 10957–10964.

(80) Liu, L.; Hunger, J.; Bakker, H. J. Energy Relaxation Dynamics of the Hydration Complex of Hydroxide. *J. Phys. Chem. A* **2011**, *115*, 14593–14598.

(81) Liu, L.; Bakker, H. J. Vibrational Excitation Induced Proton Transfer in Hydrated Nafion Membranes. *J. Phys. Chem. B* **2015**, *119*, 2628–2637.

(82) Abascal, J. L. F.; Vega, C. Widom Line and the Liquid-Liquid Critical Point for the TIP4P/2005 Water Model. *J. Chem. Phys.* **2010**, *133*, 234502.

(83) Ashihara, S.; Huse, N.; Espagne, A.; Nibbering, E. T. J.; Elsaesser, T. Ultrafast Structural Dynamics of Water Induced by Dissipation of Vibrational Energy. *J. Phys. Chem. A* **2007**, *111*, 743–746.

(84) Huse, N.; Ashihara, S.; Nibbering, E. T. J.; Elsaesser, T. Ultrafast Vibrational Relaxation of O-H Bending and Librational Excitations in Liquid H2O. *Chem. Phys. Lett.* **2005**, *404*, 389–393.

(85) Fecko, C. J.; Loparo, J. J.; Roberts, S. T.; Tokmakoff, A. Local Hydrogen Bonding Dynamics and Collective Reorganization in Water: Ultrafast Infrared Spectroscopy of HOD/D2O. *J. Chem. Phys.* **2005**, *122*, 54506.

(86) Roberts, S. T.; Ramasesha, K.; Petersen, P. B.; Mandal, A.; Tokmakoff, A. Proton Transfer in Concentrated Aqueous Hydroxide Visualized Using Ultrafast Infrared Spectroscopy. *J. Phys. Chem. A* **2011**, *115*, 3957–3972.

(87) Cringus, D.; Lindner, J.; Milder, M. T.; Pshenichnikov, M. S.; Vöhringer, P.; Wiersma, D. A. Femtosecond Water Dynamics in Reverse-Micellar Nanodroplets. *Chem. Phys. Lett.* **2005**, *408*, 162–168.

(88) Shinokita, K.; Cunha, A. V.; Jansen, T. L.; Pshenichnikov, M. S. Hydrogen Bond Dynamics in Bulk Alcohols. *J. Chem. Phys.* **2015**,

(89) Hunger, J.; Sonnleitner, T.; Liu, L.; Buchner, R.; Bonn, M.; Bakker, H. J. Hydrogen-Bond Dynamics in a Protic Ionic Liquid: Evidence of Large-Angle Jumps. *J. Phys. Chem. Lett.* **2012**, *3*, 3034–3038.

(90) Backus, E. H. G.; Nguyen, P. H.; Botan, V.; Pfister, R.; Moretto, A.; Crisma, M.; Toniolo, C.; Stock, G.; Hamm, P. Energy Transport in Peptide Helices: A Comparison between High- and Low-Energy Excitations. *J. Phys. Chem. B* **2008**, *112*, 9091–9099.

(91) Kurochkin, D. V.; Naraharisetty, S. R. G.; Rubtsov, I. V. A Relaxation-Assisted 2D IR Spectroscopy Method. *Proc. Natl. Acad. Sci.* **2007**, *104*, 14209–14214.

(92) Mackin, R. T.; Leong, T. X.; Rubtsova, N. I.; Burin, A. L.; Rubtsov, I. V. Low-Temperature Vibrational Energy Transport via PEG Chains. *J. Phys. Chem. Lett.* **2020**, 4578–4583.

(93) Botan, V.; Hamm, P. Intramolecular Vibrational Energy Relaxation in Nitrous Acid (HONO). *J. Chem. Phys.* **2008**, *129*, 164506.

(94) Kazarian, S. G.; Vincent, M. F.; Bright, F. V.; Liotta, C. L.; Eckert, C. A. Specific Intermolecular Interaction of Carbon Dioxide With Polymers. *J. Am. Chem. Soc.* **1996**, *118*, 1729–1736.

(95) Brinzer, T.; Berquist, E. J.; Dutta, S.; Johnson, C. A.; Krisher, C. S.; Lambrecht, D. S.; Garrett-Roe, S.; Ren, Z. Erratum: "Ultrafast Vibrational Spectroscopy (2D-IR) of CO2 in Ionic Liquids: Carbon Capture from Carbon Dioxide's Point of View" [J. Chem. Phys. 142, 212425 (2015)]. *J. Chem. Phys.* **2017**, *147*, 049901.

(96) Hamm, P.; Lim, M.; Hochstrasser, R. M. Vibrational Energy Relaxation of the Cyanide Ion in Water. *J. Chem. Phys.* **1997**, *107*, 10523–10531.

(97) Czurlok, D.; Gleim, J.; Lindner, J.; Vöhringer, P. Vibrational Energy Relaxation

of Thiocyanate Ions in Liquid-to-Supercritical Light and Heavy Water. A Fermi's Golden Rule Analysis. *J. Phys. Chem. Lett.* **2014**, *5*, 3373–3379.

(98) Kraack, J. P.; Hamm, P. Surface-Sensitive and Surface-Specific Ultrafast Two-Dimensional Vibrational Spectroscopy. *Chem. Rev.* **2017**, *117*, 10623–10664.

(99) Tan, H.-S.; Piletic, I. R.; Fayer, M. D. Orientational Dynamics of Water Confined on a Nanometer Length Scale in Reverse Micelles. *J. Chem. Phys.* **2005**, *122*, 174501.

(100) Ren, Z.; Kelly, J.; Gunathilaka, C. P.; Brinzer, T.; Dutta, S.; Johnson, C. A.; Mitra, S.; Garrett-Roe, S. Ultrafast Dynamics of Ionic Liquids in Colloidal Dispersion. *Phys. Chem. Chem. Phys.* **2017**, *19*, 32526–32535.

(101) Fenn, E. E.; Wong, D. B.; Fayer, M. D. Water Dynamics in Small Reverse Micelles in Two Solvents: Two-Dimensional Infrared Vibrational Echoes with Two-Dimensional Background Subtraction. *J. Chem. Phys.* **2011**, *134*, 1–11.

(102) Piletic, I. R.; Moilanen, D. E.; Spry, D. B.; Levinger, N. E.; Fayer, M. D. Testing the Core/shell Model of Nanoconfined Water in Reverse Micelles using Linear and Nonlinear IR Spectroscopy. *J. Phys. Chem. A* **2006**, *110*, 4985–4999.

(103) Fenn, E. E.; Wong, D. B.; Giammanco, C. H.; Fayer, M. D. Dynamics of Water at the Interface in Reverse Micelles: Measurements of Spectral Diffusion with Two-Dimensional Infrared Vibrational Echoes. *J. Phys. Chem. B* **2011**, *115*, 11658–11670.

(104) Zhang, Z.; Piatkowski, L.; Bakker, H. J.; Bonn, M. Interfacial Water Structure Revealed by Ultrafast Two-Dimensional Surface Vibrational Spectroscopy. *J. Chem. Phys.* **2011**, *135*.

(105) Lin, H.; Freeman, B. D. Gas and Vapor Solubility in Cross-Linked Poly(ethylene Glycol Diacrylate). *Macromolecules* **2005**, *38*, 8394–8407.

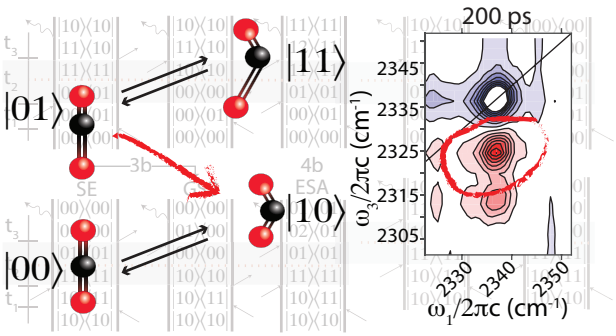
|11⟩
|01⟩
|10⟩
|00⟩
3b
SE
4b
ESA
200 ps
2345
2335
2325
2315
2305
2330
2340
2350
ω3/2πc (cm-1)
ω1/2πc (cm-1)

TOC Graphic